sustainability

MDPI

Article

Seismic Characterization of a Landslide Complex: A Case History from Majes, Peru

Jihyun Yang [1,†], Jeffrey Shragge [1,*], Aaron J. Girard [1], Edgard Gonzales [2], Javier Ticona [2], Armando Minaya [2] and Richard Krahenbuhl [1]

[1] Geophysics Department, Colorado School of Mines, Golden, CO 80401, USA; jihyuny@nvidia.com (J.Y.); agirard@mines.edu (A.J.G.); rkrahenb@mines.edu (R.K.)
[2] School of Geophysical Engineering, Universidad Nacional de San Augstín, Arequipa 04001, Peru; hgonzalesz@unsa.edu.pe (E.G.); jticonap@unsa.edu.pe (J.T.); aminayal@unsa.edu.pe (A.M.)
* Correspondence: jshragge@gmail.com
† Current address: Nvidia Corp., Austin, TX 78717, USA.

Abstract: Seismic characterization of landslides offers the potential for developing high-resolution models on subsurface shear-wave velocity profile. However, seismic methods based on reflection processing are challenging to apply in such scenarios as a consequence of the disturbance to the often well-defined structural and stratigraphic layering by the landslide process itself. We evaluate the use of alternative seismic characterization methods based on elastic full waveform inversion (E-FWI) to probe the subsurface of a landslide complex in Majes, southern Peru, where recent agricultural development and irrigation activities have altered the hydrology and groundwater table and are thought to have contributed to increased regional landslide activities that present continuing sustainability community development challenges. We apply E-FWI to a 2D near-surface seismic data set for the purpose of better understanding the subsurface in the vicinity of a recent landslide location. We use seismic first-arrival travel-time tomography to generate the inputs required for E-FWI to generate the final high-resolution 2D compressional- and shear-wave (P- and S-wave) velocity models. At distances greater than 140 m from the cliff, the inverted models show a predominantly vertically stratified velocity structure with a low-velocity near-surface layer between 5–15 m depth. At distances closer than 140 m from the cliff, though, the models exhibit significantly reduced shear-wave velocities, stronger heterogeneity, and localized shorter wavelength structure in the top 20 m. These observations are consistent with those expected for a recent landslide complex; however, follow-on geotechnical analysis is required to confirm these assertions. Overall, the E-FWI seismic approach may be helpful for future landslide characterization projects and, when augmented with additional geophysical and geotechnical analyses, may allow for improved understanding of the hydrogeophysical properties associated with suspected ground-water-driven landslide activity.

Keywords: landslide; tomography; seismic characterization; elastic full waveform inversion

check for updates

Citation: Yang, J.; Shragge, J.; Girard, A.J.; Gonzales, E.; Ticona, J.; Minaya, A.; Krahenbuhl, R. Seismic Characterization of a Landslide Complex: A Case History from Majes, Peru. *Sustainability* **2023**, *15*, 13574. https://doi.org/10.3390/su151813574

Academic Editors: Roberto Sarro and Ignacio Pérez-Rey

Received: 3 August 2023
Revised: 20 August 2023
Accepted: 21 August 2023
Published: 11 September 2023

1. Introduction

Mass wasting events such as landslides are pervasive natural hazards involving large movements of soil and rocks that can occur even in the presence of minor topography [1,2]. The social and economic costs of such events are significant, killing and injuring thousands of people each year and destroying infrastructure such as railways, highways, and tunnels [3,4]. Most landslides are triggered by rainfall or earthquakes [5,6]; However, an increasing number of cases are induced due to anthropogenic construction [7], mining [8], irrigation [9], and agricultural reclamation activities [10]. While characterizing sites prone to failure is an important geotechnical and engineering geology research area, site investigations on former landslides are not straightforward considering the disruption of structural and stratigraphic lithology imparted by the mass wasting activity.

Geophysical investigation methods provide a cost-effective solution for characterizing the subsurface structure of mass wasting events such as large-scale slumps or landslides. Since the early work of Bogoslovsky and Ogilvy [11] various geophysical techniques including seismic, electrical resistivity, and borehole analyses have been shown to be successful at site characterization before invasive site diagnosis (e.g., [12]). However, the cost of geophysical site characterization could be high due to the extensive volume of geomaterials involved in mass wasting events and the often challenging topography and complex structures induced thereby [13].

The recent development of computation resources, portable sensors such as nodal seismometers and distributed acoustic sensing (DAS) that facilitate rapid deployment, and 2D and 3D geophysical imaging and inversion algorithms position geophysical investigations as an attractive characterization tool, as shown in the increasing number of successful geophysical landslide investigations. Jongmans et al. [14] apply electrical and seismic tomography to check the rock quality and to detect instability of the slope along railway bedding. Pazzi et al. [15] show that ambient seismic wavefield measurements can be sensitive to landslides and be used to (re)construct landslide geometries. Stucchi et al. [16] present a horizontal-shear (SH)-wave depth-migrated image that profiles small slip surfaces that delineating minor landslides at shallow depths. Flamme et al. [17] present an integrated hydrological and geophysical study using electromagnetic and seismic surveys to provide insights into irrigation and landslide management.

Perhaps surprisingly to more general practitioners, seismic reflection methods are infrequently used to investigate landslides largely because the associated earth processes usually destroy established stratigraphy [18–20], which makes it challenging to record coherent reflection events in seismic data and therefore use such arrivals to both estimate the often complex velocity models and to construct interpretable seismic images. Additionally, acquiring high-resolution seismic data requires high signal-to-noise ratios and sufficiently broadband source energy, which can be challenging to realize with seismically heterogeneous and attenuative near-surface earth models. Still, seismic methods have the advantage of producing properties such as compressional- and shear-wave (P- and S-wave) velocities that directly depend on the mechanical properties important for geotechnical slope stability analysis [21,22].

This work examines how seismic data waveforms other than P-wave reflection events may offer high-resolution constraints for which seismic techniques are typically known. In addition to the more standard P-wave first-arrival refractions, we use lower-frequency (2–20 Hz) seismic waveforms typically dominated by direct and scattered surface-wave arrivals. Given the selected band of seismic data, herein we apply the following sequence of seismic inversion methods to develop high-resolution subsurface constraints: (1) first-arrival seismic refraction tomography (SRT) for P-wave velocity model estimation; and (2) low-frequency elastic full-wavefield inversion (E-FWI) to estimate the near-surface P- and S-wave velocity profiles.

We evaluate the proposed seismic inversion sequence in the context of investigating an area of active slumping and high landslide risk in the Majes region of southern Peru. The project team acquired a high-resolution near-surface 2D seismic line at an area interpreted to be at high risk for future landslide activity. For seismic data acquired on the mass wasting complex, the surface-wave arrivals are clearly affected by slower and heterogeneous velocity structures that generate strong differential moveouts and significant backscattering from suspected sub-vertical lateral discontinuities. Thus, this near-surface seismic data set offers an arguably challenging test of the combined SRT and E-FWI seismic characterization approach.

The paper begins with an overview of the geological and hydrological conditions in the Majes area. We review the near-surface geology as well as provide a brief history of irrigation and recent landslide activity. After presenting the 2D seismic data acquisition at the field site, we discuss our implementation of P-wave refraction SRT for developing starting models for the ensuing E-FWI analysis. We then present our E-FWI results, show comparisons between forward simulated and field data, and present our geological interpretations.

We conclude with discussions on the prospective improvement in surface-wave elastic time-reverse imaging strategies, the potential implications for future landslide analyses, and the importance of follow-on geotechnical analysis.

2. Majes Geology and Hydrology

The Majes I region is situated 60 km west of the regional capital Arequipa in an arid, high-altitude desert environment (see inset of Figure 1) and is one of Peru's largest agricultural developments. While meteoric water supply is limited by an average annual rainfall of 17 mm per year [23], snow melt from the Andes Mountains rising to the east provides a significant water source for agricultural irrigation and development through both the adjoining deeply incised Siguas River valley as well as a system of purpose-built irrigation aqueducts.

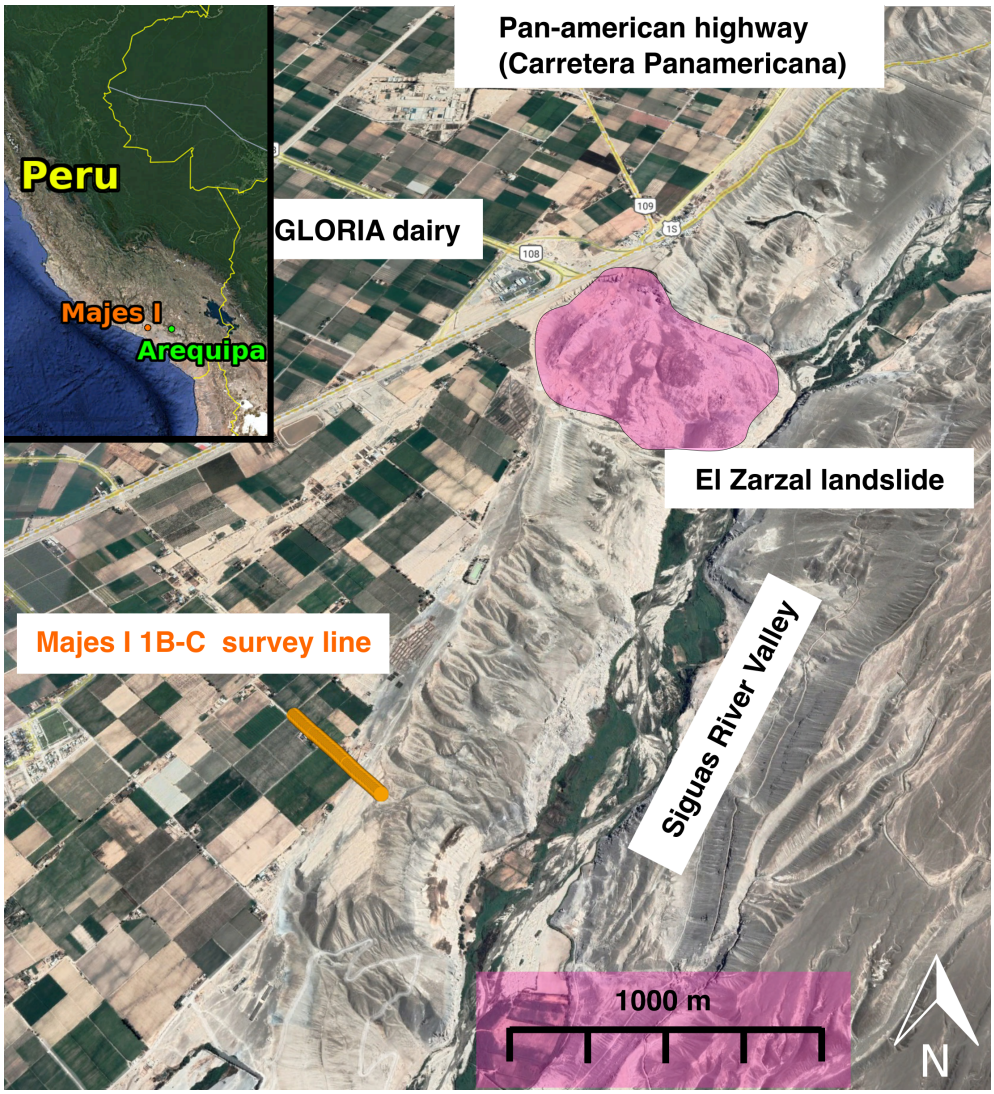

Figure 1. Satellite map of Majes I survey line 1B-C survey line with surrounding features of interest discussed in this work. The Majes 1B-C survey line is indicated in the lower left with an orange line. The location of the Pampa de Majes (Majes I) agricultural development in southern Peru can be seen in the inset at the top left.

The Majes I irrigation project has significantly contributed to the overall local food supply and created jobs; however, it also has affected the local hydrology and groundwater table and is suspected of contributing to a recent increase in landslide activities in the Siguas River valley [24–26]. In particular, after the onset of the Majes-Siguas irrigation project in

1983, initial water seepage was discovered in 1996 at the slope of the El Zarzal area. Shortly after the appearance of another seepage zone in 2004, the first significant El Zarzal landslide followed in 2005 (see highlighted magenta area in Figure 1) and failures have continued to occur causing the affected area to rapidly retreat toward the GLORIA dairy facility, agricultural fields, and Carretera Panamericana (Pan-American Highway) [17,27]. Thus, there are concerns about the overall sustainability of current irrigation-based agricultural strategy in the Majes region. Figure 1 presents a satellite image that shows the locations the El Zarzal landslide, the Pan-American Highway, the GLORIA dairy factory, as well as the particular Majes I 2D seismic survey line discussed below.

The near-surface geology at the Majes I site consists of poorly consolidated sediments including conglomerates and ignimbritic tuff [27]. The uppermost Millo conglomerate layer has an estimated thickness of 20–30 m and overlies a laterally discontinuous tuff layer of variable thickness. The underlying upper and lower Moquegua formations respectively have estimated thicknesses of 120 m and 80 m, with the upper Moquegua unit comprised of sandstones and limestone gravels and the lower Moquegua containing sandstones and clays. Water from agricultural irrigation likely percolates through the Millo unit and consequently alters the groundwater table, thus potentially contributing to the recurring El Zarzal landslide and potentially other recent events in the vicinity [25].

At the area of the current investigation, shown in Figure 2, recent water seepage is visible in the steep Siguas valley walls located downslope of the 1B-C survey line (orange dots in Figure 2). The elevation of the seepage suggests that the water table resides within the Upper Moquegua formation, which is generally competent but may be prone to failure when fully saturated [17]. Thus, the (hydro)geological parallelism with the recently time-history of the El Zarzal landslide located only 2–3 km up the Siguas River valley suggest a significantly elevated landslide risk at the field site location.

Figure 2. Satellite map of Majes I survey line 1B-C. Geophones are denoted as orange dots. The blue tinted area depicts the steeper part of the cliff face on which post-irrigation groundwater seepage is clearly visible approximately 150 m below the elevation of data acquisition surface. The Siguas River valley can be observed on the extreme right of the image.

3. Seismic Data Acquisition

A 2D near-surface seismic line was acquired in June 2022 at the field location as part of a larger multi-geophysics acquisition campaign. Figure 2 presents the acquisition geometry overlain on the satellite map. We used a 96-channel Geometrics Geode system to acquire seismic data with 14 Hz vertical-component geophones and a PEG-40 accelerated weight-drop source; geophone and source intervals were set at 5 m and 10 m, respectively. The start of the geophone line and shot points were located as close to the slope as possible

while following reasonable safety protocols regarding slope stability (to the southeast of Figure 2). The sampling rate for the recorded data was $\Delta t = 0.5$ ms with a total recording time of $T = 1.0$ s for each recorded shot gather.

Figure 3 presents two examples of 2–20 Hz bandpassed shot gathers in which direct surface-wave energy clearly dominates. We note significant backscattered energy originating around 90 m offset as well as significantly slower direct surface-wave moveouts between 0–90 m when compared to those between 90–320 m. Most other shot gathers show consistent direct surface-wave slowdowns and clearly visible backscattered surface-wave energy. Overall, these observations suggest the presence of a strong, laterally heterogeneous, velocity structure.

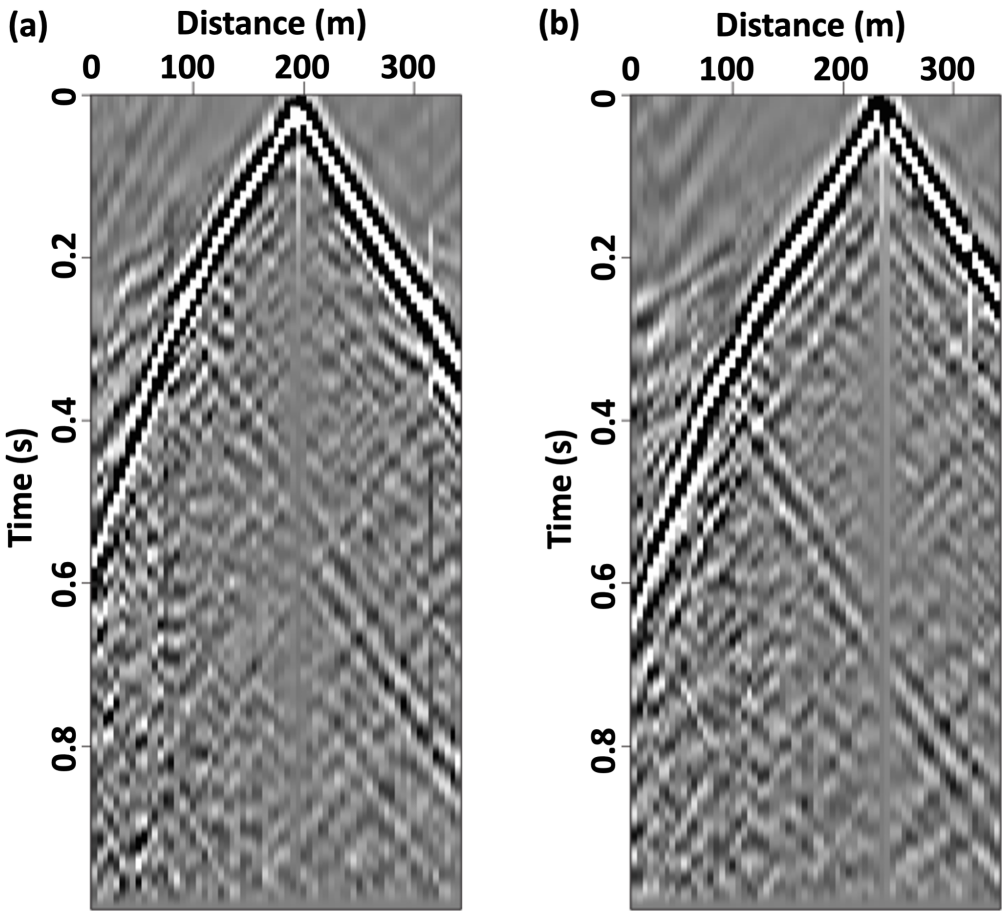

Figure 3. Examples of 2–20 Hz bandpassed shot gathers excited at (**a**) 195 m and (**b**) 235 m. Both panels exhibit a dominant direct surface wave that has backscattered energy originating at 90 m distance and significantly slower propagation between 0–90 m. Other minor scattered surface-wave events are also visible in both panels.

4. P-wave Seismic Refraction Tomography

P-wave travel-time SRT is a low-order though efficient method for generating smooth subsurface velocity models based on a picked refraction travel-time data set. SRT algorithms estimate velocity models by iteratively minimizing the difference between the observed travel times and those forward modeled through a synthetic earth model using a ray-tracing algorithm. The inversion step commonly involves solving a linearized inverse problem, usually following a numerical optimization approach.

The travel time $t_i(s,r)$ between a source s and a receiver r station (corresponding to travel-time index i) along the raypath can be computed by the summation of the travel times of the individual segments:

$$t_i(r,s) = \sum_{k=1}^{n} \frac{l_k}{v_k}, \tag{1}$$

where l_k and v_k are the path length and velocity of the kth segment between s and r, and n is the number of segments in any given raypath.

Following Ronczka et al. [28], we formulate the linearized inverse problem to obtain model parameters from travel times according to

$$\mathbf{J}\Delta\mathbf{m} = \Delta\mathbf{d} = \mathbf{d} - \mathbf{f}(\mathbf{m}), \tag{2}$$

where $\mathbf{J}$ is the Jacobian matrix of the travel times with respect to model parameters (i.e., $\partial t_i/\partial m_j$, where i is a ray index and j is grid node index); $\mathbf{m}$ is the array of velocity model parameters v_i; $\mathbf{f}(\mathbf{m})$ is the forward modeling operator; and $\mathbf{d}$ is the array of observed travel times $t_i(r,s)$ defined in Equation (1). Here, we use the shortest path method [29] with secondary nodes [30], which computes the fastest travel-time path from a source to a receiver across a specified mesh.

The seismic refraction tomography inverse problem can be solved by minimizing a regularized (i.e., smoothness-constrained) L_2-norm objective function E_{tt} [28] defined here by

$$E_{tt} = E_d + \lambda E_m = \|\mathbf{W}\Delta\mathbf{d}\|_2^2 + \lambda\|\mathbf{C}\mathbf{m}\|_2^2, \tag{3}$$

where E_d is the weighted data misfit; E_m is the model roughness; $\mathbf{W}$ is a diagonal weight matrix based on the uncertainty of travel-time picks; λ is the regularization trade-off parameter; and $\mathbf{C}$ is a derivative matrix used to calculate the model roughness. The objective function in Equation (3) is minimized using a generalized Gauss-Newton method.

We use the open-source pyGIMLi refraction travel-time tomography software [31] with the Python-based Refrapy GUI wrapper [32] for both picking P-wave first-arrival refraction travel times and solving the inverse problem. The pyGIMLi framework has been successfully applied in recent geophysical investigations [33]. We input our P-wave first-arrival picks from 16 gathers separated by a 30 m shot interval into the pyGIMLi SRT package. We use a starting model with initial values of $V_{min} = 0.5$ km/s at the surface and linearly increasing to $V_{max} = 1.2$ km/s at the 70 m model base. We set allowable velocity bounds at 0.3 km/s and 2.0 km/s, and use a $\lambda = 1000$ to bias the inversion toward a smoother model rather than over-fit the somewhat noisy P-wave refraction travel-time picks.

Figure 4 presents the estimated P-wave velocity model with a calculated relative RMS error of 5.6% after 20 iterations. The model exhibits significantly slower P-wave velocities in the top 15 m between 0 m and 130 m horizontal distance than in regions more distal from the cliff. However, because of the limited resolution afforded by SRT, we use these results as a starting model for the ensuing E-FWI analysis rather than a final interpretation model.

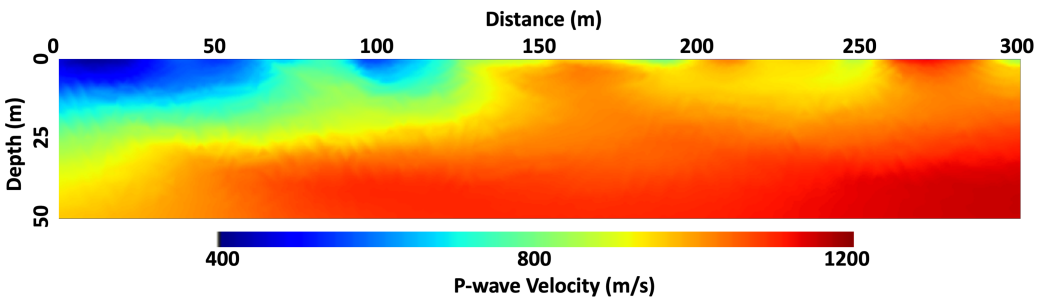

Figure 4. First-arrival P-wave travel-time tomography results, where the steep topography and Siguas River valley are located to the left of 0 m. Note the significantly slower P-wave velocity values between 0–130 m horizontal distance in the top 20 m.

5. Elastic Full Waveform Inversion

Full waveform inversion (FWI) is a commonly applied method to recover a subsurface velocity model by setting up an optimization problem based on the "goodness of fit" between forward-modeled synthetic data and observed field seismograms [34]. Because FWI has the potential for producing higher-resolution models than ray-based tomography [35,36], we expect to build a more detailed and higher-resolution velocity model after applying FWI. However, because we use surface-wave data in our FWI analysis, it is necessary to undertake an (isotropic) elastic FWI (E-FWI) analysis that enables us to forward model waveforms of this type.

We forward model seismic data by solving the 2D Cartesian isotropic elastic wave equation in a displacement-stress formulation. This involves iteratively solving two first-order system of equations: the conservation of linear momentum,

$$\rho \frac{\partial^2 u_i}{\partial t^2} = \frac{\partial \sigma_{ij}}{\partial x_j} + f_i, \tag{4}$$

and the isotropic Hooke's Law of elasticity,

$$\rho \frac{\partial \sigma_{xx}}{\partial t} = (\lambda + 2\mu)\frac{\partial u_x}{\partial x} + \lambda \frac{\partial u_z}{\partial z} + s_{xx}, \tag{5}$$

$$\rho \frac{\partial \sigma_{xz}}{\partial t} = \mu \left(\frac{\partial u_x}{\partial x} + \frac{\partial u_z}{\partial z} \right) + s_{xz}, \tag{6}$$

$$\rho \frac{\partial \sigma_{zz}}{\partial t} = \lambda \frac{\partial u_x}{\partial x} + (\lambda + 2\mu)\frac{\partial u_z}{\partial z} + s_{zz}, \tag{7}$$

where ρ, λ, and μ are the density and two isotropic Lamé parameters; u_i represents particle displacement components; σ_{ij} is the stress tensor; and f_i and s_{ij} are the force density and stress source terms, respectively.

We set up the numerical simulation grid with the spatial and temporal sampling intervals of $\Delta x = \Delta z = 1.0$ m and $\Delta t = 5 \times 10^{-5}$ s, respectively. We enforce the free-surface boundary condition on the top face and apply a ten-point perfectly matched layer (PML) boundary condition [37] to the left, right and bottom model boundary regions. The overall model dimension is 350 m $\times$ 72 m excluding the PML regions.

We formulate the E-FWI problem to minimize the commonly used L_2 norm data misfit [34,38,39] here represented by

$$E = \frac{1}{2} \sum_{N_S} \sum_{N_R} \int_0^T \|\Delta \mathbf{d}(\mathbf{s}, \mathbf{r}, t)\|^2 \, \mathrm{d}t, \tag{8}$$

where for E-FWI we define $\Delta \mathbf{d} = \mathbf{d}_{obs} - \mathbf{d}_{mod}$ as the data residual vector representing the difference between the observed and forward modeled data; and N_S and N_R are the number of source and receiver points, respectively. To estimate the velocity model that minimizes the objective function in Equation (8), we apply the adjoint-state method to define the gradient with respect to the model parameters

$$\delta \mathbf{m}'(\mathbf{X}) = \frac{\partial E}{\partial \mathbf{m}} = \sum_{N_S} \int_0^T \sum_{N_R} \left[\frac{\partial u}{\partial \mathbf{m}} \right]^* \delta u_i^\dagger \, \mathrm{d}t, \tag{9}$$

where $\left[\frac{\partial u}{\partial \mathbf{m}} \right]^*$ is the Fréchet derivative; and $\delta u_i^\dagger$ is the adjoint wavefield variable reconstructed by injecting and backpropagating information in data residual vector $\mathbf{\Delta d}$. It is possible to estimate the gradient with respect to the target S-wave velocity model parameter using the Fréchet derivative, as has been demonstrated in classical work on 2D elastic scattered wavefield inversion [34,40,41].

We use a velocity-density (V_p, V_s, ρ) E-FWI parameterization shown by Köhn et al. [42] to provide more accurate inversion results with fewer artifacts than Lamé (λ, μ, ρ) or seismic

impedance (I_p, I_s, ρ) formulations. We then use the estimated S-wave gradient at each iteration to update the S-wave velocity model $\mathbf{V_S}$ following the steepest-descent formulation,

$$\mathbf{V_S}^{(k+1)} = \mathbf{V_S}^{(k)} - \alpha \frac{\partial E^{(k)}}{\partial \mathbf{V_S}} = \mathbf{V_S}^{(k)} - \alpha \Delta \mathbf{V_S}^{(k)}, \tag{10}$$

where α is the calculated step length using parabolic fitting method [43,44]; the (k) superscripts indicate iteration number; and $\Delta \mathbf{V_S}^{(k)}$ is the estimated gradient vector.

2D E-FWI on Majes I Field Data

We now apply the above E-FWI framework to reconstruct a high-resolution S-wave velocity model for the Majes I 1B-C data set. The Majes 1B-C seismic survey line is one of many acquired in the Majes I region. This line starts at the steepening cliff face and ends at 1B along a dirt road within the agricultural fields. We initially updated the S-wave velocity model parameter with a global optimization approach that used all frequencies simultaneously in the 2–20 Hz range; however, we observed that the data-difference misfit function suffered from local-minima issues [34,45] and converged more poorly than expected. To mitigate this local minima problem, we adopted a multiscale approach [46] by which we increased the maximum frequency of the data sequentially in frequency subsets between 2–20 Hz (i.e., covering the dominant surface-wave frequency band). After conducting a number of tests, we split the inversion process into the four frequency sub-bands: 2–7 Hz, 2–12 Hz, 2–17 Hz, and 2–20 Hz.

We used a first-derivative Gaussian wavelet with a center frequency of 20 Hz bandpassed between 2–20 Hz as our source wavelet, which enabled a good match of the modeled frequency content to that of the dominant field-data frequency band. To improve the phase matching between the observed and modeled waveforms, we applied a source-wavelet correction filter estimated through linearly damped least-squares optimization [47]. This source-estimation approach approximated a wavelet appropriate for each frequency sub-band.

To build an isotropic E-FWI starting model, we use a smoothed version of the P-wave velocity model obtained from P-wave first-arrival travel-time SRT (Figure 5) and then approximate the S-wave velocity model (not shown) by assuming a Poisson solid (i.e., $V_S = V_P/\sqrt{3}$). We hold the homogeneous density model constant during the inversion due to a lack of *a priori* information on this parameter.

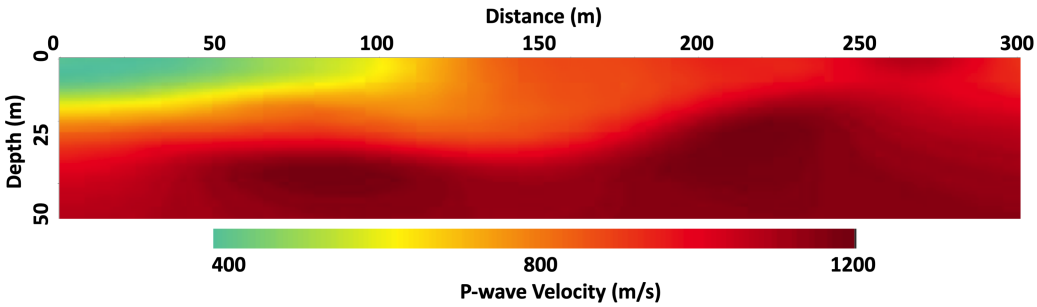

Figure 5. The starting V_P velocity model generated from P-wave first arrival travel-time SRT. Note that the starting V_S model is given by a Poisson solid approximation (i.e., $V_S = V_P/\sqrt{3}$).

To illustrate the convergence of E-FWI, Figure 6 presents the relative errors of models with iterations. As shown in Figure 6, the E-FWI analysis has converged by approximately 45 iterations. Due to the multiscale approach, the error curve exhibits a staircase-like structure, which is caused by the loss decreasing quickly at the beginning of each frequency sub-band discussed above.

We first show synthetic data generated through from the final estimated E-FWI model as a grayscale image in Figure 7 and overlay the observed data in wiggle-plot format. This representation facilitates comparison between the observed and forward modeled synthetic data, and is a visual representation of the differences that the E-FWI framework aims to

minimize through model updating. Figure 7a,b respectively present overlay plots of shot gathers acquired at 215 m and 255 m. Both panels show coherent waveforms as direct and backscattered surface waves at locations throughout the panels.

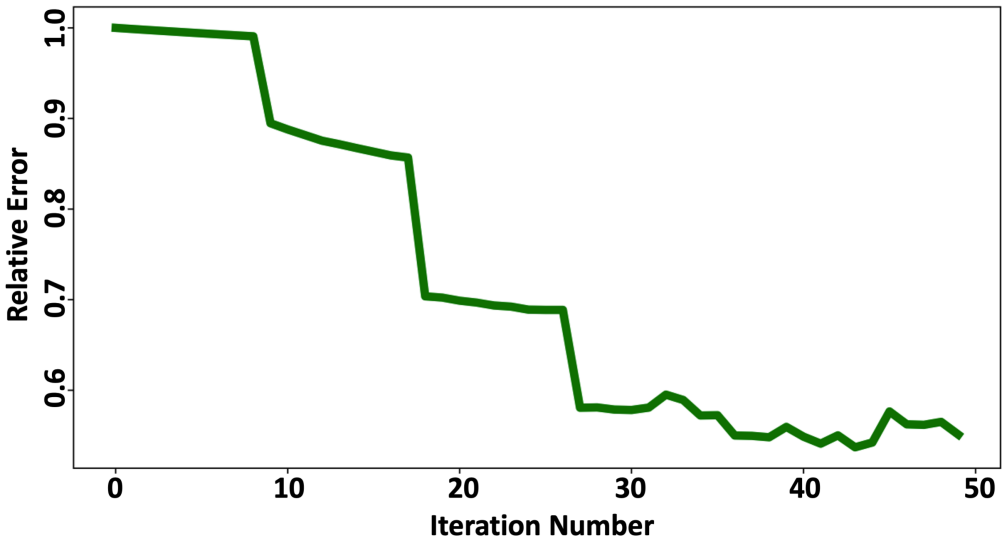

Figure 6. Normalized objective function for E-FWI iteration. Note that the step-like discontinuities represent points where the inversion algorithm progressed to the next frequency sub-band for E-FWI analysis.

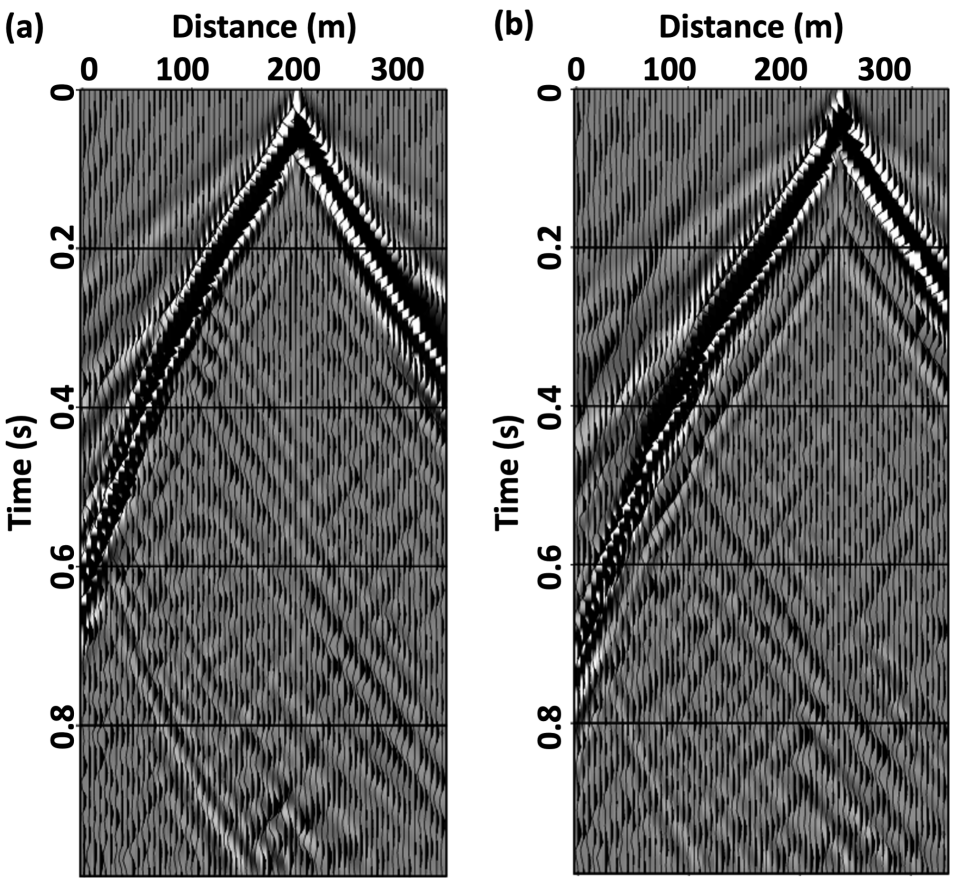

Figure 7. Overlay of forward-model data (gray scale) and observed seismic waveforms (wiggle-trace plot) for shot gathers located at (**a**) 215 m and (**b**) 255 m horizontal distance.

Figure 8a presents the resulting estimated V_S model from the E-FWI inversion, which has been updated significantly from the initial tomographic model. At distances greater

than 130 m, we observe that the estimated V_S model exhibits largely vertically dominant model structure. Moving downward from the surface, we interpret a 6–8 m thick layer with average V_S velocity of 0.55 km/s overlying a 6–8 m thick layer with average V_S velocity of 0.35 km/s; these two layers likely are associated with the Millo formation. At approximately 16–18 m depth, we note a significant V_S increase to about 0.70 km/s, which may be associated with a tuff layer and/or the upper Moquegua formations. Using these observation, we divide the estimated V_S model into layers by black dashed lines, representing the potential interfaces between the interpreted layers (see Figure 8b).

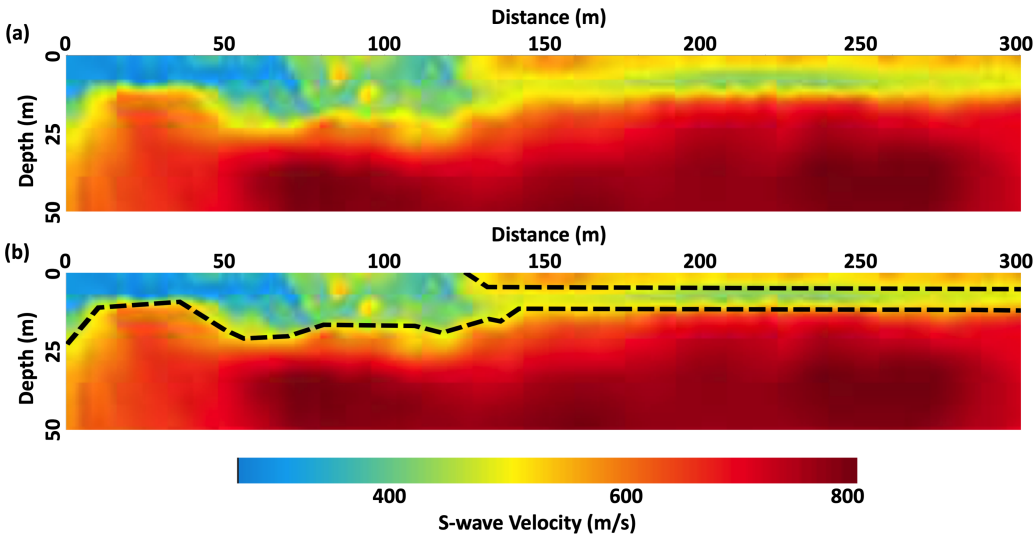

Figure 8. (**a**) The E-FWI estimated V_S model and (**b**) associated overlain interpretations with units demarcated by dotted lines. At distances beyond 130 m, the estimated model is mostly 1D with a 6–8 m layer with an average velocity of $V_S = 0.55$ m/s overlaying a 6–8 m layer with a 0.35 km/s velocity. The V_S model shows significant differences at horizontal distances of 0.0–0.13 km. Within the top 0.02 km, the estimated V_S model is slower at 0.25–0.40 km/s, suggesting reduced shear modulus values with potentially less compacted and poorly sorted conglomerate materials. The inverted V_S model between 0.07–0.13 km appears to have both stronger and shorter-wavelength heterogeneity.

Between 0 m and 130 m horizontal distance, though, the estimated V_S model is significantly different than that from 130 m to the end of the survey line. We observe significantly slower V_S values between 0.25 km/s and 0.40 km/s from the surface down to 20 m depth. We note that careful consideration should be given to the challenges of geological and geotechnical interpretations of geophysical imaging and inversion results. Here, we interpret the lateral variability of the observed velocity changes (and associated reductions in shear moduli) are consistent with what would be expected in a former large-scale slump (or perhaps former historical landslide) complex zone characterized by less compacted and more poorly sorted conglomerate materials. The character of the inverted V_S model between 0.075–0.10 km distance also appears to exhibit stronger and short-wavelength heterogeneity. At depths greater than 20 m, though, the V_S values increase and approach those observed at these depths elsewhere in the S-wave velocity section, suggesting a possible base of suspected mass wasting activity. However, additional geotechnical investigation would be required to confirm these interpretations and determine the underlying causes and mechanisms that may have triggered the observed large-scale slumping (and perhaps historical landslide) activity.

6. Discussion

This study illustrates that the combination of P-wave first-arrival SRT and E-FWI can provide valuable subsurface constraints for seismic characterization of mass wasting complexes. However, it is important to recognize that this approach falls within in a spectrum of possible

analyses that support subsurface characterization efforts and have their respective merits and drawbacks. Here, we highlight five complementary, non-destructive seismic approaches able to provide subsurface constraints on the S-wave velocity profile: (1) horizontal-vertical spectral ratio (HVSR) [48]; (2) spectral analysis of surface waves (SASW) [49]; (3) multichannel analysis of surface waves (MASW) [50]; (4) SH-wave seismic refraction tomography (SH-SRT) [51]; and (5) SRT+E-FWI presented herein.

1. HVSR uses ambient multicomponent seismic records to develop S-wave model constraint. While this approach requires a limited data set and is highly numerically efficient, it also is generates low-resolution 1D constraints though pseudo 2D sections can be estimated by interpolating the results of neighboring independent HVSR measurements.
2. SASW uses single-component data from multiple receivers to characterize shallow S-wave profiles. While this approach also requires a limited data set and is highly numerically efficient, it is limited to 1D (or pseudo-2D) analyses and suffers from several limitations that arise due to seismic wavefields being comprised of more wavefield phases than the fundamental Rayleigh mode.
3. MASW uses waveforms from a receiver array to address some of the issues arising in SASW; however, this approach requires additional acquisition resources and provides an spatially averaged 1D S-wave velocity profile beneath the array (though pseudo-2D sections can be generated).
4. SH-SRT uses first-arrival energy generated by a SH-wave source and seismic data acquired on shear geophones to estimate a 2D S-wave velocity profile of somewhat low resolution. This approach requires additional acquisition resources, involves picking arrivals, and involves higher computational requirements.
5. The SRT+FWI method reported herein uses geophone array data to develop a fully 2D high-resolution S-wave velocity model estimate. Compared to the four previous methods, though, this approach is significantly more computationally challenging, demands careful data preprocessing, requires reasonably accurate starting models, and is not guaranteed to converge to the global minimum.

Thus, practitioners should carefully weigh the advantages and potential drawbacks of the different seismic methods when looking to generate S-wave velocity constraints on the near-surface geologic profile. Fortunately, there is a range of possibilities that can be tailored to the technical requirements at hand, the availability of seismic acquisition instrumentation, the availability of computing hardware and software, and the skill sets of personnel involved in the seismic survey and ensuing analysis.

Potential Research Opportunities

Combining different geophysical techniques for studying large-scale slumping and landslide environments is known to be useful for improved characterization [52]; thus, we expect that integrating these results with other geophysical methods (e.g., DC resistivity) would more effectively constrain hydrogeophysical factors such as saturation and variability in the water table depth [17] and could provide a more complete calibration and thorough investigation of this large-scale slump (and perhaps historical landslide) complex.

Given the high-quality backscattered surface-wave arrivals, it may be possible to develop an elastic time-reverse imaging algorithm that could generate images of the discontinuities generating the scattered surface-wave energy. Ideally, these seismic waveform types could be used to directly detect former failure surfaces and/or other sub-vertical velocity discontinuities associated with historical landslide activities. Moreover, detecting sub-vertical model discontinuities could be useful for improved geotechnical understanding of their contribution to future failures and the associated landslide risk.

Successfully applying near-surface geophysical methods on former landslides remains generally challenging because these energetic events are affected by a variety of geologic, topographic, geomorphologic, and hydrologic factors. While the deployment of additional sensors would require extra effort under strongly variable topography, we expect that multi-component geophones or an alternative sensing system such as DAS could improve

upon the types of data and ensuing results present herein. Furthermore, DAS would enable cost-effective solutions for survey design that could leverage the dense temporal and spatial spacing to provide higher-resolution characterization of sub-vertical velocity heterogeneity.

While seismic inversion provides velocity models for estimating shear moduli, identifying the underlying causes and failure mechanisms of suspected landslides remains challenging because mapping shear-modulus observations to actual soil strength is not a straightforward task. There is a large body of geotechnical research into mapping landslide vulnerability and investigating landslide mechanisms. For example, additional stability analysis of the failure stage can reveal the failure mechanisms and the ensuing mass movement, which can be used to classify landslide type (e.g., rotational or flow). Thus, a supplemental follow-up study by geotechnical specialists is recommended for more a complete characterization of this large-scale mass wasting complex.

Finally, we emphasize that the seismic methodology highlighted here is not limited to landslide evaluation. Rather, there are a number of geotechnical areas of focus in which such a methodology likely would apply. Important examples include periodic evaluation of the internal structural health of mine tailings dams, analyzing the slope stability and open-pit mines, and performing higher-resolution site characterization studies in advance of developing civil infrastructure.

7. Conclusions

We present a two-step seismic inversion procedure for characterizing a suspected recent landslide complex using a 2D near-surface seismic data set acquired at a field site of high landslide potential in Majes, southern Peru. The observed seismic waveforms in the 2–20-Hz frequency band are dominated by direct surface-wave arrivals, which carry the imprint of significant lateral velocity variations and backscattered surface-wave energy from numerous points along the transect.

We use first-arrival P-wave refraction travel-time picks to build a P-wave velocity seismic refraction tomography (SRT) model and then employ this result in an elastic full-waveform inversion (E-FWI) analysis to construct the final high-resolution models. We show that the estimated S-wave velocity model is significantly updated using surface-wave energy dominant in the 2–20 Hz frequency band. The resulting E-FWI S-wave model exhibits characteristics consistent with former geologic studies at this site and generate forward-modeled wavefields that achieve a sufficient waveform fit with field data observations. At distances farther than 130 m from the cliff face, the inversion results reveal an earth model dominated by a vertical velocity structure; however, at closer distances we observe significantly slower S-wave values and isolated strong 2D velocity heterogeneity in the top 20 m.

While these observations are consistent with those expected in a recent mass wasting (and perhaps historical landslide) complex, we stress the need for follow-on geotechnical analysis to confirm these assertions. Overall, we expect this combined seismic inversion toolkit could be helpful for future (suspected) landslide characterization projects, though perhaps augmented with complementary geophysical analyses (e.g., DC resistivity) more sensitive to (hydro)geophysical properties associated with potentially groundwater-driven landslide activity.

Author Contributions: Conceptualization, J.S. and J.Y.; methodology, J.Y., J.S. and A.J.G.; software, J.Y. and J.S.; validation, J.Y., J.S., R.K. and A.J.G.; formal analysis, J.Y., J.S. and R.K.; investigation, J.Y. and J.S.; resources, R.K., J.S., E.G., J.T. and A.M.; data curation, J.Y. and J.S.; writing—original draft preparation, J.Y. and J.S.; writing—review and editing, all; visualization, J.Y. and J.S.; supervision, J.S., A.J.G. and R.K.; project administration, R.K., E.G., A.M., J.T. and J.S.; funding acquisition, R.K., E.G., A.M., J.T. and J.S. All authors have read and agreed to the published version of the manuscript.

Funding: This work was funded in part by the Center for Mining Sustainability, a joint venture between the Universidad Nacional de San Augustin de Arequipa (Peru) and the Colorado School of Mines (USA).

Institutional Review Board Statement: Not applicable.

Informed Consent Statement: Not applicable.

Data Availability Statement: Data are available by contacting the authors.

Acknowledgments: The authors thank the valuable contributions from the Center for Mining Sustainability, Arequipa, Peru. We thank the sponsors of the Mines Center for Wave Phenomena (CWP), whose funding support made this research possible (JY). We acknowledge the support of the CSM CIARC HPC group and the use of the CSM Wendian Cluster resources. The reproducible numerical examples and plots in this paper were developed using the Madagascar (https://www.ahay.org) and Python-based Matplotlib software packages.

Conflicts of Interest: The authors declare no conflict of interest.

Abbreviations

The following abbreviations are used in this manuscript:

2D	Two-dimensional
CSM	Colorado School of Mines
DAS	Distributed Acoustic Sensing
DC	Direct Current
E-FWI	Elastic full waveform inversion
E-TRI	Elastic time reverse imaging
HVSR	Horizontal-vertical spectral ratio
FWI	Full waveform inversion
MASW	Multichannel analysis of surface waves
P wave	Compressional wave
PML	Perfectly matched layer
SASW	Spectral analysis of surface waves
SH wave	Horizontal shear wave
S wave	Shear wave
SRT	Seismic refraction tomography
UNSA	Universidad Nacional de San Augstín

References

1. Fan, X.; Scaringi, G.; Korup, O.; West, A.J.; van Westen, C.J.; Tanyas, H.; Hovius, N.; Hales, T.C.; Jibson, R.W.; Allstadt, K.E.; et al. Earthquake-Induced Chains of Geologic Hazards: Patterns, Mechanisms, and Impacts. *Rev. Geophys.* **2019**, *57*, 421–503. [CrossRef]
2. Tanyaş, H.; Görüm, T.; Kirschbaum, D.; Lombardo, L. Could road constructions be more hazardous than an earthquake in terms of mass movement? *Nat. Hazards* **2022**, *112*, 639–663. [CrossRef]
3. Schuster, R.L.; Highland, L. *Socioeconomic and Environmental Impacts of Landslides in the Western Hemisphere*; US Department of the Interior, US Geological Survey: Denver, CO, USA, 2001.
4. Guzzetti, F. Landslide Hazard and Risk Assessment. Ph.D. Thesis, Universitäts-und Landesbibliothek, Bonn, Germany, 2006.
5. Van Westen, C.J.; Castellanos, E.; Kuriakose, S.L. Spatial data for landslide susceptibility, hazard, and vulnerability assessment: An overview. *Eng. Geol.* **2008**, *102*, 112–131. [CrossRef]
6. Lepore, C.; Kamal, S.A.; Shanahan, P.; Bras, R.L. Rainfall-induced landslide susceptibility zonation of Puerto Rico. *Environ. Earth Sci.* **2012**, *66*, 1667–1681. [CrossRef]
7. Zhang, Y.; Yang, J.; Yang, F. Field investigation and numerical analysis of landslide induced by tunneling. *Eng. Fail. Anal.* **2015**, *47*, 25–33. [CrossRef]
8. Salmi, E.F.; Nazem, M.; Karakus, M. Numerical analysis of a large landslide induced by coal mining subsidence. *Eng. Geol.* **2017**, *217*, 141–152. [CrossRef]
9. Lacroix, P.; Dehecq, A.; Taipe, E. Irrigation-triggered landslides in a Peruvian desert caused by modern intensive farming. *Nat. Geosci.* **2020**, *13*, 56–60. [CrossRef]
10. Li, Y.; Wang, X.; Mao, H. Influence of human activity on landslide susceptibility development in the Three Gorges area. *Nat. Hazards* **2020**, *104*, 2115–2151. [CrossRef]
11. Bogoslovsky, V.; Ogilvy, A. Geophysical methods for the investigation of landslides. *Geophysics* **1977**, *42*, 562–571. [CrossRef]
12. Mahmood, K.; ur Rehman, Z.; Farooq, K.; Memon, S.A. One dimensional equivalent linear ground response analysis — A case study of collapsed Margalla Tower in Islamabad during 2005 Muzaffarabad Earthquake. *J. Appl. Geophys.* **2016**, *130*, 110–117. [CrossRef]

13. Aleotti, P.; Chowdhury, R. Landslide hazard assessment: Summary review and new perspectives. *Bull. Eng. Geol. Environ.* **1999**, *58*, 21–44. [CrossRef]
14. Jongmans, D.; Demanet, D.; Havenith, H.; Hemroulle, P. Application of 2D electrical and seismic tomography techniques for investigating landslide sites. In Proceedings of the 5th EEGS-ES Meeting, Budapest, Hungary, 6–9 September 1999; European Association of Geoscientists & Engineers: Utrecht, The Netherlands, 1999; p. cp–35 .
15. Pazzi, V.; Tanteri, L.; Bicocchi, G.; D'Ambrosio, M.; Caselli, A.; Fanti, R. H/V measurements as an effective tool for the reliable detection of landslide slip surfaces: Case studies of Castagnola (La Spezia, Italy) and Roccalbegna (Grosseto, Italy). *Phys. Chem. Earth Parts A/B/C* **2017**, *98*, 136–153. [CrossRef]
16. Stucchi, E.; Tognarelli, A.; Ribolini, A. SH-wave seismic reflection at a landslide (Patigno, NW Italy) integrated with P-wave. *J. Appl. Geophys.* **2017**, *146*, 188–197. [CrossRef]
17. Flamme, H.E.; Krahenbuhl, R.A.; Li, Y.; Dugan, B.; Shragge, J.; Graber, A.; Sirota, D.; Wilson, G.; Gonzales, E.; Ticona, J. Integrated geophysical investigation for understanding agriculturally induced landslides in southern Peru. *Environ. Earth Sci.* **2022**, *81*, 1–14. [CrossRef]
18. Jongmans, D.; Garambois, S. Geophysical investigation of landslides: A review. *Bull. Société Géologique Fr.* **2007**, *178*, 101–112. [CrossRef]
19. Ferrucci, F.; Amelio, M.; Sorriso-Valvo, M.; Tansi, C. Seismic prospecting of a slope affected by deep-seated gravitational slope deformation: The Lago Sackung, Calabria, Italy. *Eng. Geol.* **2000**, *57*, 53–64. [CrossRef]
20. Bichler, A.; Bobrowsky, P.; Best, M.; Douma, M.; Hunter, J.; Calvert, T.; Burns, R. Three-dimensional mapping of a landslide using a multi-geophysical approach: The Quesnel Forks landslide. *Landslides* **2004**, *1*, 29–40. [CrossRef]
21. Hack, R. Geophysics for slope stability. *Surv. Geophys.* **2000**, *21*, 423–448. [CrossRef]
22. Uhlemann, S.; Hagedorn, S.; Dashwood, B.; Maurer, H.; Gunn, D.; Dijkstra, T.; Chambers, J. Landslide characterization using P-and S-wave seismic refraction tomography—The importance of elastic moduli. *J. Appl. Geophys.* **2016**, *134*, 64–76. [CrossRef]
23. Wei, X.; Garcia-Chevesich, P.; Alejo, F.; García, V.; Martínez, G.; Daneshvar, F.; Bowling, L.C.; Gonzáles, E.; Krahenbuhl, R.; McCray, J.E. Hydrologic analysis of an intensively irrigated area in southern Peru using a crop-field scale framework. *Water* **2021**, *13*, 318. [CrossRef]
24. Lacroix, P.; Araujo, G.; Hollingsworth, J.; Taipe, E. Self-Entrainment Motion of a Slow-Moving Landslide Inferred From Landsat-8 Time Series. *J. Geophys. Res. Earth Surf.* **2019**, *124*, 1201–1216. [CrossRef]
25. Graber, A.; Santi, P.; Radach, K.; Meza Arestegui, P.; Chacon Arcaya, S. Finite element model calibration in the context of limited data and limited access: A case study from a large landslide in Southern Peru. In Proceedings of the 54th US Rock Mechanics/Geomechanics Symposium, Golden, Colorado, USA, 28 June–1 July 2020; OnePetro: Richardson, TX, USA, 2020.
26. Graber, A.; Santi, P.; Meza Arestegui, P. Constraining the critical groundwater conditions for initiation of large, irrigation-induced landslides, Siguas River Valley, Peru. *Landslides* **2021**, *18*, 3753–3767. [CrossRef]
27. Araujo Huamán, G.E.; Taipe Maquerhua, E.L.; Miranda Cruz, R.; Valderrama Murillo, P.A. *Dinámica y Monitoreo del Deslizamiento de Siguas*; Minero y Metalúrgico—INGEMMET, Informe Técnico, N° A6748; Región Arequipa, provincia Caylloma y Arequipa, distrito Majes y San Juan de Siguas, Instituto Geológico: San Juan de Siguas, Peru, 2017 .
28. Ronczka, M.; Hellman, K.; Günther, T.; Wisén, R.; Dahlin, T. Electric resistivity and seismic refraction tomography: A challenging joint underwater survey at Äspö Hard Rock Laboratory. *Solid Earth* **2017**, *8*, 671–682. [CrossRef]
29. Moser, T. Shortest path calculation of seismic rays. *Geophysics* **1991**, *56*, 59–67. [CrossRef]
30. Giroux, B.; Larouche, B. Task-parallel implementation of 3D shortest path raytracing for geophysical applications. *Comput. Geosci.* **2013**, *54*, 130–141. [CrossRef]
31. Rücker, C.; Günther, T.; Wagner, F.M. pyGIMLi: An open-source library for modelling and inversion in geophysics. *Comput. Geosci.* **2017**, *109*, 106–123. [CrossRef]
32. Guedes, V.J.C.B.; Maciel, S.T.R.; Rocha, M.P. Refrapy: A Python program for seismic refraction data analysis. *Comput. Geosci.* **2022**, *159*, 105020. [CrossRef]
33. Mollaret, C.; Wagner, F.M.; Hilbich, C.; Scapozza, C.; Hauck, C. Petrophysical joint inversion applied to alpine permafrost field sites to image subsurface ice, water, air, and rock contents. *Front. Earth Sci.* **2020**, *8*, 85. [CrossRef]
34. Virieux, J.; Operto, S. An overview of full-waveform inversion in exploration geophysics. *Geophysics* **2009**, *74*, WCC1–WCC26. [CrossRef]
35. Robein, E. *Seismic Imaging: A Review of the Techniques, their Principles, Merits and Limitations (EET 4)*; EAGE Publications: Houten, The Netherlands, 2010.
36. Schuster, G.T. *Seismic Inversion*; Society of Exploration Geophysicists: Tulsa, OK, USA, 2017.
37. Komatitsch, D.; Martin, R. An unsplit convolutional perfectly matched layer improved at grazing incidence for the seismic wave equation. *Geophysics* **2007**, *72*, SM155–SM167. [CrossRef]
38. Gélis, C.; Virieux, J.; Grandjean, G. Two-dimensional elastic full waveform inversion using Born and Rytov formulations in the frequency domain. *Geophys. J. Int.* **2007**, *168*, 605–633. [CrossRef]
39. Sears, T.J.; Singh, S.; Barton, P. Elastic full waveform inversion of multi-component OBC seismic data. *Geophys. Prospect.* **2008**, *56*, 843–862. [CrossRef]
40. Mora, P. Nonlinear two-dimensional elastic inversion of multioffset seismic data. *Geophysics* **1988**, *52*, 1211–1228. [CrossRef]

41. Tromp, J.; Tape, C.; Liu, Q. Seismic tomography, adjoint methods, time reversal and banana-doughnut kernels. *Geophys. J. Int.* **2005**, *160*, 195–216. [CrossRef]
42. Köhn, D.; De Nil, D.; Kurzmann, A.; Przebindowska, A.; Bohlen, T. On the influence of model parametrization in elastic full waveform tomography. *Geophys. J. Int.* **2012**, *191*, 325–345. [CrossRef]
43. Nocedal, J.; Wright, S.J. Quadratic programming. In *Numerical Optimization*; Springer, New York, NY, USA, 2006; pp. 448–492.
44. Métivier, L.; Bretaudeau, F.; Brossier, R.; Operto, S.; Virieux, J. Full waveform inversion and the truncated Newton method: quantitative imaging of complex subsurface structures. *Geophys. Prospect.* **2014**, *62*, 1353–1375. [CrossRef]
45. Hu, W.; Chen, J.; Liu, J.; Abubakar, A. Retrieving low wavenumber information in FWI: An overview of the cycle-skipping phenomenon and solutions. *IEEE Signal Process. Mag.* **2018**, *35*, 132–141. [CrossRef]
46. Bunks, C.; Saleck, F.M.; Zaleski, S.; Chavent, G. Multiscale seismic waveform inversion. *Geophysics* **1995**, *60*, 1457–1473. [CrossRef]
47. Groos, L.; Schäfer, M.; Forbriger, T.; Bohlen, T. The role of attenuation in 2D full-waveform inversion of shallow-seismic body and Rayleigh waves. *Geophysics* **2014**, *79*, R247–R261. [CrossRef]
48. Nakamura, Y. Method for dynamic characteristics estimation of subsurface using microtremor on the ground surface. *Railw. Tech. Res. Inst. Q. Rep.* **1989**, *30*, 25–33.
49. Heisey, J.; Stokoe, K.; Meyer, A. Moduli of pavement systems from Spectral analysis of surface waves. *Transp. Res. Rec.* **1982**, *852*, 22–31.
50. Park, C.B.; Miller, R.D.; Xia, J. Multichannel analysis of surface waves. *Geophysics* **1999**, *64*, 800–808. [CrossRef]
51. Chen, J.; Zelt, C.; Jaiswal, P. Detecting a known near-surface target through application of frequency-dependent traveltime tomography and full-waveform inversion to P- and SH-wave seismic refraction data. *Geophysics* **2017**, *82*, R1–R17. [CrossRef]
52. Grandjean, G.; Gourry, J.C.; Sanchez, O.; Bitri, A.; Garambois, S. Structural study of the Ballandaz landslide (French Alps) using geophysical imagery. *J. Appl. Geophys.* **2011**, *75*, 531–542. [CrossRef]